https://doi.org/10.5194/egusphere-2026-3044
Preprint. Discussion started: 4 June 2026

Structural warming biases distort extreme rainfall intensification estimates in event attribution

Damián Insua-Costa[1], Marc Lemus-Cánovas[2], Martín Senande-Rivera[3], Victoria M. H. Deman[1], João L. Geirinhas[1], and Diego G. Miralles[1]

[1]Hydro-Climate Extremes Lab, Ghent University, 9000 Ghent, Belgium
[2]Center for Climate Change and Transformation, Eurac Research, 39100 Bolzano/Bozen, Italy
[3]Mitiga Solutions, 08002 Barcelona, Spain
Correspondence: damian.insuacosta@ugent.be

Abstract. Extreme event attribution (EEA) is becoming an increasingly important component of climate change risk assessment and communication. While most EEA methods rely on numerical models, the extent to which model fidelity in representing anthropogenic warming shapes attribution outcomes remains underexplored. Here we identify global-scale biases in leading CMIP6 climate models relative to reanalysis data and show that these biases directly propagate into EEA results. CMIP6 models reproduce the integrated magnitude of anthropogenic warming but systematically distort its three-dimensional structure, underestimating lower-tropospheric warming over land—thus dampening land–sea thermal contrasts—while overestimating upper-tropospheric warming, particularly in the Northern Hemisphere. Consequently, in a storyline-based testbed experiment for the October 2024 Valencia storm (Spain), the response in extreme rainfall rises from ∼10 % under CMIP6-derived warming to ∼30 % under an observationally constrained signal. This enhanced response is driven by increased low-level moistening, larger convective instability, and strengthened upper-level winds that push precipitation well beyond Clausius–Clapeyron scaling. We also show similar structural mismatches across multiple Northern Hemisphere mid-latitude locations, suggesting that this underestimation is not event-specific. Our results underscore the need to strengthen confidence in attribution methods and provide a robust pathway for constructing observationally constrained counterfactual climates.

1 Introduction

The intensification of extreme weather is one of the most evident expressions of anthropogenic climate change, with heavy precipitation among its most damaging outcomes (Allan and Soden, 2008; Min et al., 2011; Donat et al., 2016). This trend, consistently documented in successive IPCC assessment reports (Masson-Delmotte et al., 2021), has raised both scientific and societal concern over how global warming is reshaping the risks associated with high-impact weather. In this context, extreme event attribution (EEA) has emerged as a key approach to quantify the human influence on specific extremes (Stott et al., 2016; Shepherd, 2016; Clarke et al., 2022). EEA builds on physical understanding and quantitative analysis to ask a fundamental question: how this same event would have manifested in the absence of anthropogenic warming, in terms of both frequency and severity. Beyond its scientific relevance, attribution also plays a crucial role in communicating the impacts of climate change, bridging the gap between complex climate processes and societal perception of risk (Sillmann et al., 2021).

A broad range of EEA methodologies have been developed to tackle this question, most of which rely on ensembles of factual (present-day) and counterfactual (pre-industrial) simulations to quantify how anthropogenic forcing alters the likelihood and intensity of a given event. These methodologies span a continuum of approaches, from risk-based analyses that quantify probability changes (Stott et al., 2004; Pall et al., 2011), to methods based on circulation analogues (Cattiaux et al., 2010; Faranda et al., 2022) and storylines that construct physically consistent counterfactuals (Shepherd et al., 2018; van Garderen et al., 2021). Despite their diversity, most ultimately rely on climate models to simulate the anthropogenic warming signal that distinguishes the two worlds. The credibility of EEA outcomes therefore depends on how well these models reproduce the observed temperature change.

Yet, in practice, global climate models, including those from the Coupled Model Intercomparison Project Phase 6 (CMIP6) (Eyring et al., 2016), exhibit well-documented biases in representing regional temperature patterns (Ossó et al., 2023; Zebaze et al., 2025) and the vertical profile of atmospheric warming, such as the well-known positive bias in tropical tropospheric temperature trends (Masson-Delmotte et al., 2021; Santer et al., 2005; Thorne et al., 2011; Mitchell et al., 2020). However, little attention has been paid to how these model errors may propagate into EEA frameworks. In particular, in extreme event storylines, anthropogenic warming signals from CMIP6 models are typically incorporated in attribution simulations in one of two ways. The event of interest can be simulated directly within a global climate model, using either a CMIP6 model itself (Sánchez-Benítez et al., 2022; Athanase et al., 2024) or another Earth system model that inherits the CMIP6 forcing and boundary conditions to construct counterfactual scenarios (John et al., 2026; Campos et al., 2025). Alternatively, the warming signal can be extracted from CMIP6 models and used to perturb the initial and/or boundary conditions of a higher-resolution model, following the pseudo-global warming (PGW) approach (Schär et al., 1996; Insua-Costa et al., 2024; Calvo-Sancho et al., 2026). In both cases, it is implicitly assumed that the CMIP6-derived temperature trend accurately represents the observed structure of warming, including its vertical distribution and regional contrasts. Whether systematic deviations in the spatial pattern of this trend can substantially influence the attribution of individual extreme events remains largely unexplored.

Here, we address this gap by examining the global-scale biases in CMIP6 warming patterns relative to observationally constrained reanalysis data from ERA5 (Hersbach et al., 2020), focusing on both the vertical and horizontal dimensions of the temperature response. We then assess how these differences affect EEA outcomes using a storyline framework, where storyline attribution is implemented through pseudo-global-warming simulations conducted in the Model for Prediction Across Scales (MPAS) (Skamarock et al., 2012). Within this framework, we apply both CMIP6- and ERA5-derived anthropogenic signals to simulate a high-impact precipitation event: the infamous October 2024 storm over Valencia (Spain), which caused severe flooding and more than 200 fatalities (AEMET, 2024).

2 Data and methods

2.1 Warming signals

To characterize the anthropogenic warming structure used in our experiments, we combined simulations from CMIP6 (Eyring et al., 2016) with the ERA5 reanalysis (Hersbach et al., 2020). We focus on a small but representative subset of six CMIP6 models—CESM2-WACCM, BCC-CSM2-MR, EC-Earth3, GFDL-ESM4, MPI-ESM1-2-HR, and MRI-ESM2-0—spanning major climate modelling centres in North America, Europe, and Asia (Table S1). Although not exhaustive, this subset captures key dimensions of model diversity and comprises models that are among the most widely used in contemporary global and regional climate assessments, ensuring that the ensemble reflects the warming structures typically employed in attribution studies. Hereafter, "CMIP6" refers to this six-model ensemble. For the validation analyses we work with the multi-model mean, while for the attribution experiments (Sect. 2.3) the warming signal of each individual model is applied separately to construct one counterfactual simulation per model.

For each model, the anthropogenic warming signal was derived by combining the historical and intermediate-emissions Shared Socioeconomic Pathway (SSP) 2-4.5 simulations for 2015–2024. Although the CMIP6 historical simulations begin in 1850, we compute temperature trends starting in 1940, as this is the first year available in ERA5, which serves as our benchmark dataset. The resulting 1940–2024 trend fields were calculated for air temperature at multiple pressure levels to evaluate both the vertical and horizontal structures of warming. The same procedure was applied to ERA5 by computing linear temperature trends over 1940–2024 and multiplying them by the number of years to obtain the total warming signal. CMIP6 warming patterns are validated against ERA5, and the resulting CMIP6−ERA5 difference is hereafter referred to as the model "bias". We acknowledge that ERA5 is not a direct observation and carries its own uncertainties, particularly in the early decades and over data-sparse regions; however, we adopt it as our benchmark because it represents the state-of-the-art in global reanalysis and is the most widely used reference in the climate community. The robustness of our comparison against an alternative reanalysis (NCEP/DOE) is documented in Sect. 3.1.

2.2 Attribution framework

For the validation, both datasets rely on annual-mean trends. However, for the EEA experiments, the CMIP6 anthropogenic signals used to perturb the model follow the standard pseudo-global warming procedure (Schär et al., 1996): the warming field is defined as the difference between the 30-year mean centred on the event year (2009–2039) and the corresponding pre-industrial baseline (1850–1880), both computed from monthly mean temperatures. For ERA5, which does not extend to the pre-industrial period, we do derive the present-day warming signal by multiplying the 1940–2024 linear trend in monthly-mean temperature by 85 years, yielding an estimate of anthropogenic warming relative to 1940. For both ERA5 and CMIP6, the monthly warming signals are linearly interpolated to daily resolution to align the imposed warming pattern with the simulated event.

The resulting perturbations were subsequently applied within a storyline framework (Shepherd et al., 2018; van Garderen et al., 2021) to quantify the influence of global warming on the Valencia storm. Only thermodynamic fields were modified, including three-dimensional air temperature and specific humidity, together with surface variables such as sea-surface temperature, skin temperature, 2-m air temperature, and 2-m dew-point temperature. Specific humidity was not directly perturbed; instead, a constant-relative-humidity assumption was adopted, allowing specific humidity to adjust instantaneously to the imposed temperature perturbation. Dynamical variables (winds and geopotential) were kept unchanged to preserve the event's synoptic structure. However, although dynamical fields were not initially perturbed, they respond to the new thermodynamic state: geopotential heights rise under warming, and winds adjust to the modified temperature and, consequently, pressure gradients.

Mathematically, the perturbed field in the counterfactual simulation (X_C) is expressed as

$$X_C = X_F - \Delta X, \tag{1}$$

where X_F denotes the factual field and ΔX the signal derived from CMIP6 or ERA5. This framework enables a controlled comparison between two alternative representations of the anthropogenic signal—one model-based and one observation-constrained—allowing assessment of how structural biases in the imposed warming pattern influence extreme rainfall in the simulated Valencia case.

To quantify the differences between factual and counterfactual experiments, the relative change between F and C is reported as

$$\Delta = \frac{F - C}{F} \times 100\,\%, \tag{2}$$

i.e. normalised by the factual event rather than by the counterfactual one. This choice differs from the more common convention $(F - C)/C$ used in some attribution studies, but has two advantages. First, F provides a single reference state that is shared by all counterfactual experiments, both CMIP6- and ERA5-based, allowing their results to be displayed on a common scale. Second, the resulting Δ has a direct interpretation as "the fraction of the factual event attributable to anthropogenic warming". Where appropriate, we report values under the alternative $(F - C)/C$ normalisation in Sect. 4 to facilitate comparison with other attribution studies. Throughout the analysis, each counterfactual member is compared with the factual member sharing the same initialisation date and time, so that the resulting Δ captures the response to the imposed thermodynamic perturbation alone and is not contaminated by synoptic variability across initialisations (Sect. 2.3).

2.3 MPAS simulations

All simulations were performed with the Model for Prediction Across Scales (MPAS) (Skamarock et al., 2012), configured with a variable-resolution mesh ranging from 60 km globally to 3 km over the western Mediterranean (Fig. S2). MPAS simulations employed the Grell–Freitas cumulus scheme (Grell and Freitas, 2014), the WRF single-moment 6-class (WSM6) microphysics scheme (Hong and Lim, 2006), and the Yonsei University (YSU) planetary boundary-layer parameterization (Hong et al., 2006). This configuration captures both the large-scale synoptic flow and the mesoscale convective structures responsible for extreme precipitation. The initial conditions for the factual simulations were taken from ERA5, while counterfactual simulations were initialized with perturbed versions of these fields based on the anthropogenic warming signals from either CMIP6 or ERA5, as described above.

Each experiment consisted of a nine-member ensemble using a lagged-initialization approach, with start times every three hours from 00 UTC 27 October to 00 UTC 28 October 2024. This sampling strategy captures internal variability in the event's evolution: the earliest member begins two days before the main day of the rainfall episode (29 October), and the latest one day prior. All simulations end on 30 October at 00:00 UTC, meaning that their duration ranges between 2 and 3 days. Thanks to the daily interpolation of the perturbation fields (Sect. 2.2), each counterfactual member is perturbed with the values corresponding to its specific initialisation date. The factual ensemble thus includes nine members, mirrored by nine ERA5-based counterfactual runs. The CMIP6 counterfactual set combines the nine initialization times with the six CMIP6 warming signals, yielding 54 simulations. Additionally, we ran nine future simulations, obtained by adding (rather than subtracting) the ERA5 warming signal to the initial conditions, representing a plausible near-future climate. In total, 81 MPAS integrations were performed (9 factual + 9 ERA5-past counterfactual + 54 CMIP6-past counterfactual + 9 ERA5-future counterfactual). Unless explicitly qualified, “ERA5 counterfactual” and “CMIP6 counterfactual” refer to the past variants throughout the manuscript. Model outputs include precipitation, temperature, and winds, but also diagnostics such as column-integrated water vapour (IWV) or convective available potential energy (CAPE), providing insight into the thermodynamic and dynamical mechanisms modulated by the imposed warming patterns. For the ensemble analyses, statistical significance is evaluated using a two-tailed one-sample t-test against the null hypothesis that the spatially aggregated difference between factual and counterfactual simulated variables equals zero. Significance is assessed under a dual criterion: the p-value must pass a given threshold and the absolute signal-to-noise ratio (mean over standard deviation across ensemble members) must be at least 1, so that trivially small signals are not flagged as significant.

This MPAS-based storyline framework builds on the approach previously applied to the August 2022 Mediterranean derecho (González-Alemán et al., 2023), here extended with a much larger ensemble and with the addition of the observationally constrained ERA5-based attribution branch.

3 Results

3.1 Global biases in the three-dimensional structure of atmospheric warming

The vertical distribution of anthropogenic warming is broadly consistent between CMIP6 models and the ERA5 reanalysis, both showing a clear and widespread warming signal across the global troposphere (Fig. 1). In both datasets, the strongest warming appears near the Arctic surface, reflecting Arctic amplification mainly driven by both the lapse-rate feedback and the surface-albedo feedback associated with sea-ice loss (Pithan and Mauritsen, 2014). A second warming maximum is evident in the tropical upper troposphere, where moist deep convection maintains a near-moist-adiabatic temperature profile. As surface temperatures rise, convection transports larger amounts of water vapour upward, enhancing latent heating through condensation and leading to a proportionally stronger warming aloft than at the surface, a response that is further amplified by the water-vapour feedback. These agreements indicate that, despite some differences among individual members (Figs. S3 and S4), CMIP6 models realistically capture the first-order structure of the atmospheric temperature response to greenhouse forcing. This conclusion is robust to the inclusion of the 2015–2024 SSP2-4.5 segment in CMIP6: when both datasets are compared over their common historical-only period (1940–2014), the spatial patterns and biases are closely aligned (Fig. S5).

https://doi.org/10.5194/egusphere-2026-3044
Preprint. Discussion started: 4 June 2026

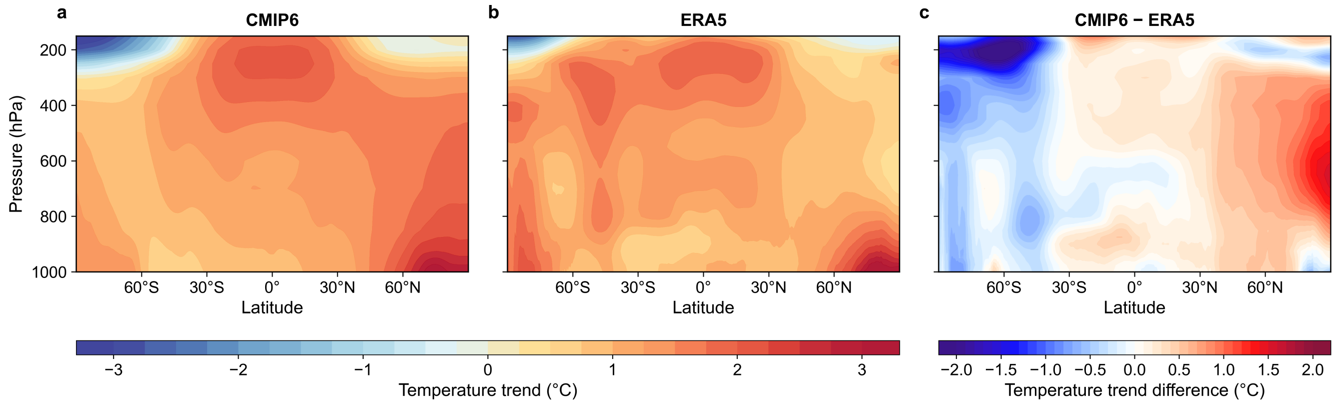

Figure 1. (a) Zonal-mean air-temperature trend from the CMIP6 multi-model mean computed over 1940–2024 and expressed as the total warming over the 85-year period (°C). (b) Same as (a) but from ERA5. (c) Difference CMIP6 − ERA5. Trends are calculated from annual-mean temperatures at standard pressure levels between 1000 and 150 hPa.

However, systematic differences emerge in the magnitude and vertical gradients of this warming. CMIP6 models exhibit a stronger amplification in the tropical upper troposphere than ERA5, consistent with previous findings that attribute this behaviour to convective parameterizations that redistribute latent heat too efficiently and thus overestimate warming aloft (Keil et al., 2021). The positive bias extends through the mid-latitudes of the Northern Hemisphere and intensifies toward the Arctic. Here, model-simulated turbulent mixing has been shown to be systematically too strong in stable boundary-layer regimes (Davy and Esau, 2014), smoothing vertical temperature gradients and amplifying warming in mid- to upper-tropospheric layers while dampening warming at the Arctic surface.

By contrast, the Southern Hemisphere exhibits a weaker warming signal in CMIP6 than in ERA5, although the interpretation of this difference is inherently more uncertain due to the limited observational coverage over the Southern Ocean and Antarctica, particularly in the early decades of the ERA5 record (Soci et al., 2024). However, recent work has shown evidence of Antarctic amplification, with surface temperatures over the continent increasing more rapidly than simulated by current climate models, suggesting that CMIP6 may underestimate the forced warming in high southern latitudes (Casado et al., 2023). This hemispheric contrast may also reflect biases in large-scale heat transport, with models potentially redistributing heat too efficiently toward the Northern Hemisphere relative to the Southern Hemisphere.

To further investigate these biases, we examine the horizontal structure of warming at different atmospheric levels (Fig. 2), which reveals key regional differences. In the upper troposphere (Fig. 2a, d), the CMIP6 ensemble shows the strongest warming magnitudes across much of the tropics, particularly over the eastern tropical Pacific, the tropical Atlantic, tropical Africa, and the western Indian Ocean. ERA5 also exhibits substantial upper-tropospheric tropical warming, but the pattern is more heterogeneous, with localized maxima embedded within regions of more moderate warming. At mid-tropospheric levels (Fig. 2b, e), this contrast remains: ERA5 displays a more spatially variable structure, whereas CMIP6 produces a more regionally coherent and amplified warming signal, especially across the Northern Hemisphere mid-latitudes and the Arctic sector. This

https://doi.org/10.5194/egusphere-2026-3044
Preprint. Discussion started: 4 June 2026

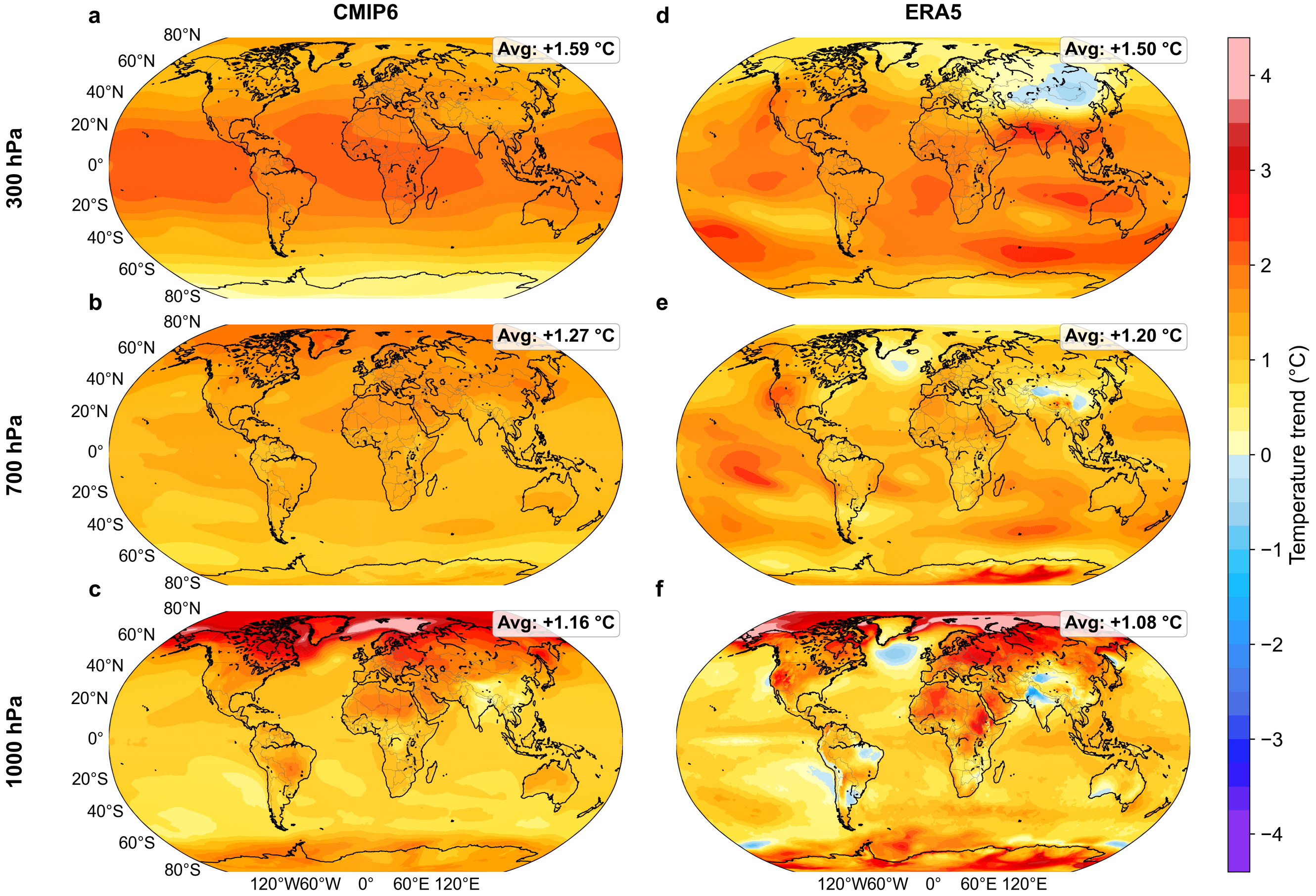

Figure 2. Air-temperature trend (°C) from the CMIP6 multi-model mean and ERA5 at 300, 700 and 1000 hPa, 1940–2024.

oversmoothed structure in CMIP6 likely reflects ensemble averaging, coarser resolution, and simplified process representation, including cloud-related processes, which remain a major source of uncertainty in climate models.

Near the surface (Fig. 2c, f), both datasets reproduce Arctic amplification, although CMIP6 overestimates warming over Greenland and underestimates it over the Arctic Ocean, while also capturing Antarctic amplification with lower magnitude than ERA5. In the Northern Hemisphere mid-latitudes, CMIP6 models fail to represent several known regional warming hotspots, including the western North American coast and the Mediterranean basin, both across western Europe and northern Africa, likely reflecting limitations in reproducing land–atmosphere coupling, whereby excessive soil moisture and latent heat flux in the model dampen surface sensible heating (Mueller and Seneviratne, 2014; Yuan and Quiring, 2017). Over the oceans, CMIP6 and ERA5 are broadly consistent, though CMIP6 does not capture features such as the cold blob south of Greenland (Fan et al., 2024). When globally averaged (see annotations in Fig. 2), CMIP6 exhibits a warm bias below 0.1 °C across all levels, indicating that despite regional deviations the models retain strong skill in representing the planet-wide temperature

https://doi.org/10.5194/egusphere-2026-3044
Preprint. Discussion started: 4 June 2026

185 trend. Finally, although our assessment uses ERA5 as the primary benchmark due to its state-of-the-art status and widespread use, similar large-scale trend patterns are found in other reanalysis such as NCEP/DOE Reanalysis II (Fig. S6) and JRA-55 (Simmons, 2022), providing further support for the robustness of our validation.

3.2 Propagation of model warming biases into attribution

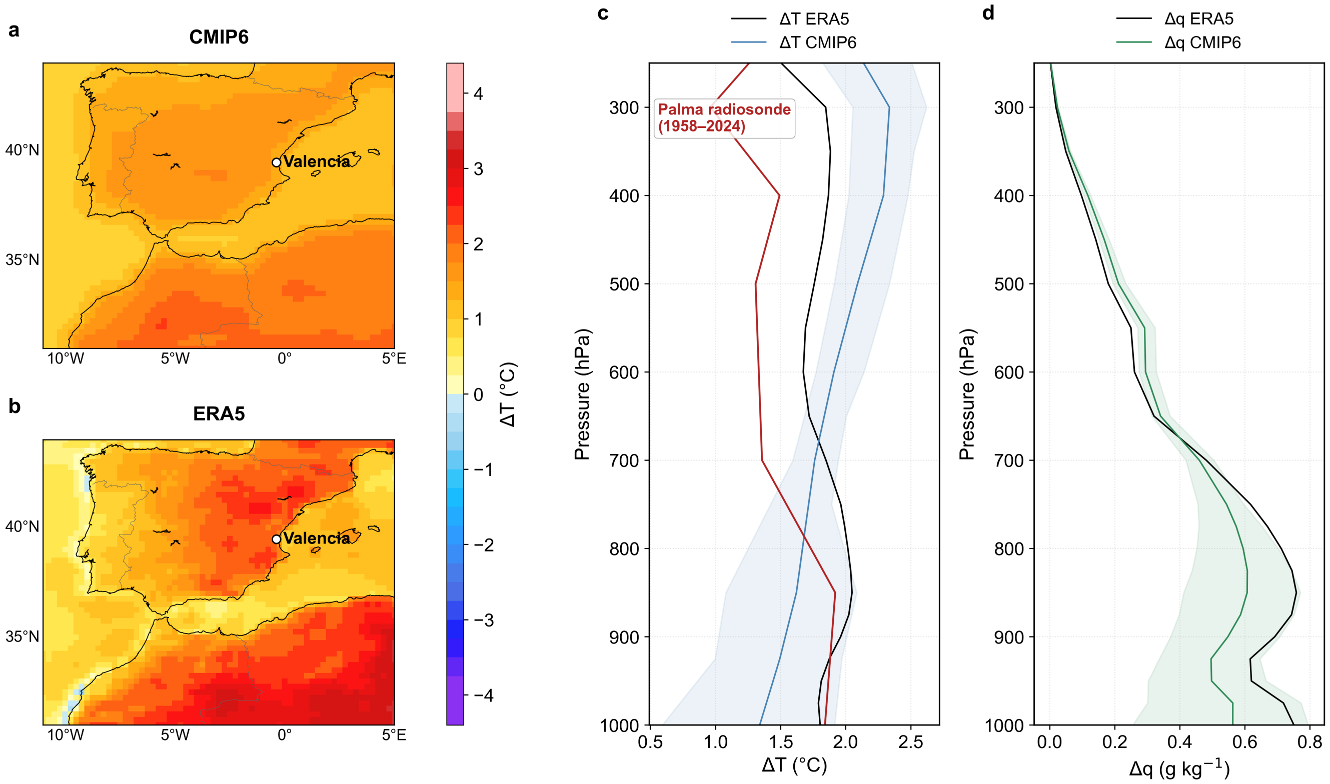

Figure 3. (a) Surface temperature perturbation ΔT over the western Mediterranean using the CMIP6 warming signal. (b) Same as (a) for ERA5. (c, d) Vertical profiles of ΔT and Δq at the Valencia point, including the Palma de Mallorca radiosonde trend (1958–2024) as independent in-situ reference (red).

This section examines how the large-scale warming biases described above translate into the local warming signal used 190 for EEA, focusing on the western Mediterranean region where the October 2024 Valencia storm occurred (Fig. 3). Unlike Figs. 1 and 2, which show annual-mean trends, Fig. 3 displays the warming perturbations actually imposed in the attribution simulations, as described in Methods. As shown in Fig. 2f, the western Mediterranean exhibits amplified surface warming with distinct signatures when comparing CMIP6 models to ERA5, making it an ideal test bed to assess how differences in the imposed warming pattern influence EEA outcomes.

https://doi.org/10.5194/egusphere-2026-3044
Preprint. Discussion started: 4 June 2026

Fig. 3 compares key thermodynamic fields perturbed in our experiments: skin temperature (Fig. 3a, b) and the vertical profiles of temperature and specific humidity (Fig. 3c, d). All warming signals shown in Fig. 3 are interpolated to 27 October, the initialisation date of the majority of our ensemble members. At the surface, the ERA5-derived signal shows stronger land warming, particularly east of the Iberian Peninsula and across northern Africa. In contrast, CMIP6 exhibits weaker warming over land and somewhat stronger warming over the adjacent ocean relative to ERA5. Although land warming remains larger than ocean warming in both datasets, this pattern results in a more spatially homogeneous warming field and a markedly reduced land–sea thermal contrast in CMIP6.

The vertical temperature profiles over Valencia (Fig. 3c) further highlight the structural differences between CMIP6 and ERA5. The ERA5 profile exhibits two distinct warming maxima—one in the lower troposphere (∼850 hPa) and a secondary one near 300 hPa in the upper troposphere. In contrast, CMIP6 produces reduced warming below ∼700 hPa and progressively stronger warming with height, yielding a smooth, single-peaked profile that maximizes near 300 hPa. As an independent observational benchmark, we also include the temperature trend from the Palma de Mallorca radiosonde (1958–2024; red line in Fig. 3c). Although the radiosonde record starts later than the ERA5 and CMIP6 trends used here (1940–2024), the comparison remains informative for assessing the realism of the imposed vertical structure. Below ∼850 hPa the Palma profile is in close agreement with ERA5, both showing maximum warming in the lower troposphere; above this level Palma warms less than ERA5 and substantially less than CMIP6. The qualitative shape of the Palma profile—with a clear lower-tropospheric maximum—thus matches ERA5 and contrasts with the CMIP6 multi-model mean, which peaks aloft, reinforcing the validity of our ERA5-based approach. The Palma site is approximately 250 km from Valencia, sufficiently close for the radiosonde to be representative of the regional warming structure.

Because most atmospheric water vapour resides in the lower troposphere, the vertical structure of warming directly shapes the moistening profile. The strong low-level warming in ERA5 (Fig. 3c) drives a substantial increase in lower-tropospheric specific humidity (Fig. 3d), whereas the weaker low-level warming in CMIP6 yields a much smaller moistening response, even though the warming in CMIP6 is larger at higher altitudes. The contrast between vertical profiles also implies different temperature lapse-rate responses: stronger low-level warming combined with weaker upper-level warming, as in ERA5—and even more so in the Palma radiosonde—steepens the lapse rate and enhances convective instability, while the CMIP6 profile, with maximum warming aloft, has the opposite effect. Crucially, the Palma radiosonde combines a low-level warming comparable to ERA5 with an even weaker upper-level warming, which would translate into a similar low-level moistening but a steeper lapse rate, suggesting that the ERA5-based signal used here may even be on the conservative side.

3.3 Sensitivity of extreme rainfall attribution to warming structure

Here we examine the results of the attribution simulations conducted with MPAS (Fig. 4), which quantify the degree to which the different anthropogenic perturbations described above modulate simulated extreme precipitation responses. The maps show ensemble-mean conditions on the main day of the event (29 October), including 500-hPa geopotential height (shading), sea-level pressure (contours), and 24-hour accumulated precipitation. The factual ensemble (Fig. 4a) exhibits the characteristic circulation pattern associated with extreme rainfall in eastern Spain: a pronounced cut-off low (DANA) aloft, centred north of

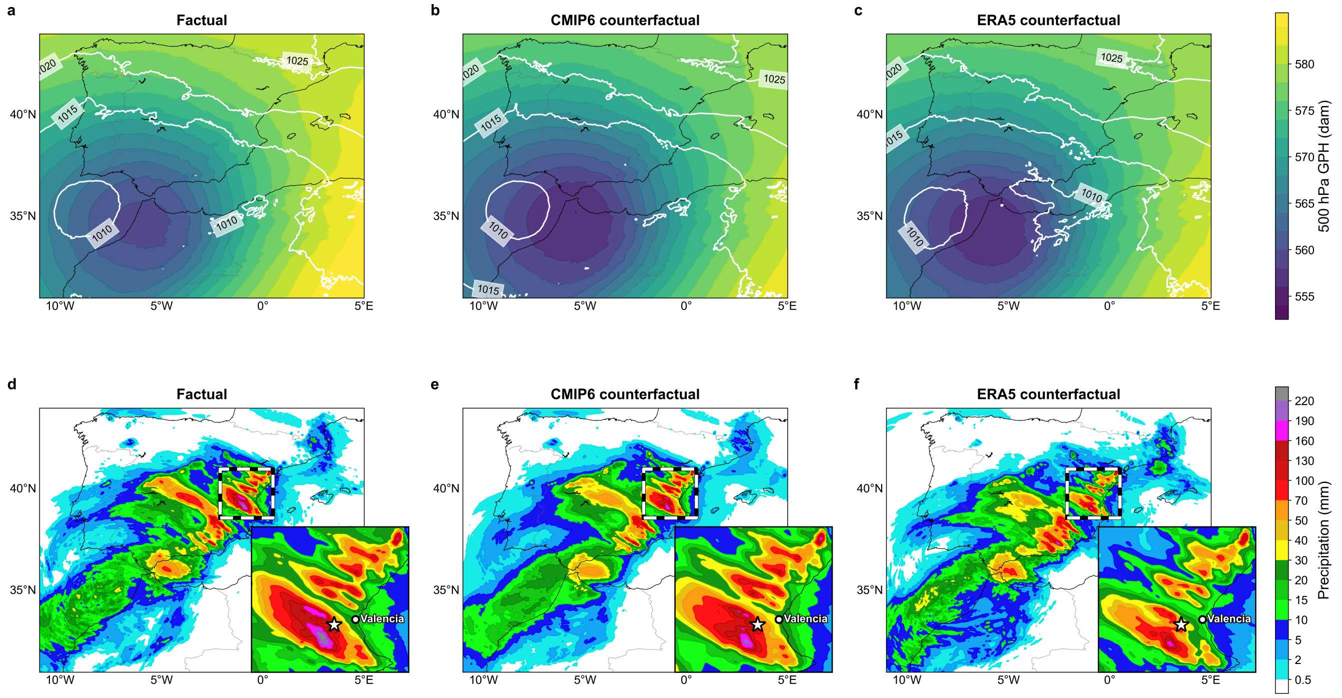

Figure 4. (a–c) Mean 500-hPa geopotential height (colours, dam) and mean sea-level pressure (contours, hPa) at 12 UTC on 29 October 2024 for the factual ensemble (a), the CMIP6-past counterfactual (b) and the ERA5-past counterfactual (c). (d–f) 24-h accumulated precipitation (mm) for the same experiments, with a zoom-in over the Valencian region; the star marks Turís (Valencia), where the storm peak was recorded.

Morocco, generating upper-level divergence and broad-scale ascent over the western Mediterranean. Near the surface, a low-pressure system sustains persistent easterly onshore flow, which channels a warm and humid Mediterranean air mass toward the Valencian coast, establishing a highly favourable convective environment.

In the counterfactual ensembles (Fig. 4b, c), where the anthropogenic warming signal is removed using either the CMIP6-derived or ERA5-derived pattern, the overall synoptic configuration is retained. The cut-off low and the associated low-level easterlies remain, reflecting the storyline approach in which the large-scale dynamical setting of the event is preserved while allowing thermodynamic adjustment. Consistent with the cooler background state, geopotential heights are lower in both counterfactual simulations. The magnitude of this reduction, which is representative of the layer-mean temperature, is similar for the CMIP6- and ERA5-based perturbations, indicating that although the vertical structure of the imposed warming differs substantially between the two signals (Fig. 3c), their column-integrated thermal effect is comparable.

The spatial pattern of precipitation in the factual ensemble (Fig. 4d) closely resembles the observed distribution of rainfall associated with the event (AEMET, 2024). The simulations reproduce the narrow precipitation corridor affecting the Valencian interior, and the location of the simulated rainfall maximum lies very close to the observed peak in Turís (Valencia) (AEMET, 2024), albeit slightly displaced to the southwest. While the model does not capture the observed 24-hour maximum exceeding

https://doi.org/10.5194/egusphere-2026-3044
Preprint. Discussion started: 4 June 2026

700 mm (AEMET, 2024), it does generate extreme accumulations above 200 mm in the ensemble mean and localized peaks exceeding 300 mm in individual members, indicating that beyond capturing the spatial structure of the event, the model is able to simulate convective intensities consistent with a high-impact rainfall episode.

In the counterfactual ensembles (Fig. 4e, f), the differences in accumulated precipitation reveal a clear sensitivity to the spatial structure of the imposed warming signal. In the simulation where the anthropogenic component is removed using the CMIP6-derived warming pattern, daily precipitation totals remain similar to those in the factual ensemble, with limited reduction in the area of extreme rainfall (see lower-right zoom panels). By contrast, the counterfactual simulation using the ERA5-derived warming pattern produces a substantially weaker event, with a broad reduction in rainfall over the region most affected by flooding, reflected in the marked weakening of the highest precipitation intensities. Although local exceptions exist, when integrated over the southern half of the Iberian Peninsula as a whole, the reduction in accumulated precipitation remains statistically larger in the ERA5-based counterfactual than in the CMIP6-based one (Figs. S7 and S8).

3.4 Thermodynamic and dynamical mechanisms shaping the attribution response

Fig. 5a, b show the relative change in daily-accumulated precipitation on 29 October 2024 between the factual and counterfactual ensembles, expressed in terms of the spatial mean (Pmean) and spatial maximum (Pmax) precipitation over the Valencian Community (Fig. S7). Pmean is proportional to the total volume of water fallen over the domain, while Pmax captures the storm peak. With the CMIP6-based perturbation, the increase from preindustrial to present conditions remains modest, with a median change of $+6\,\%$ (IQR $[-4,+13]$) in Pmean and $+13\,\%$ (IQR $[-2,+21]$) in Pmax. In contrast, when the warming signal is derived from ERA5, the increase is substantially larger, reaching $+34\,\%$ (IQR $[+29,+47]$) for Pmean and $+30\,\%$ (IQR $[+23,+38]$) for Pmax. Although differences between mean and peak values lie within ensemble variability, both metrics provide a consistent picture: the anthropogenic contribution to rainfall intensity is small with CMIP6 ($\sim$10 %) and substantial with ERA5 ($\sim$30 %), and exhibits much stronger ensemble agreement in the latter.

Fig. 5c, d illustrate the thermodynamic factors underlying these differences. In the CMIP6-based experiments, IWV increases by a median of $+11\,\%$, accompanied by a similar increase in CAPE ($+12\,\%$). The increase in IWV is consistent with a warming of approximately 1.5 °C (albeit distributed differently with height; Fig. 3c), and the corresponding increases in CAPE and precipitation of similar magnitude suggest a moisture-driven thermodynamic amplification, broadly following Clausius–Clapeyron scaling. In contrast, the ERA5-based perturbations yield a stronger CAPE increase ($+28\,\%$), consistent with greater low-level warming and moistening than in CMIP6. Despite similar daily-mean IWV increases, the stronger pre-convective morning IWV enhancement in ERA5 (16 % vs. 11 % in CMIP6; Fig. S9) helps explain the larger CAPE and rainfall increases.

Fig. 5e, f show that the dynamical response also differs. While the CMIP6-based experiments display minimal changes in wind speed at either low or upper levels, the ERA5-based perturbations yield a significant strengthening of upper-level winds (median $+13\,\%$), while near-surface winds remain largely unchanged. This vertical wind change is consistent with a stronger land–sea thermal contrast in the ERA5 warming signal (Fig. 3b), enhancing the horizontal temperature gradient and thus intensifying the upper-level flow as a direct consequence of thermal-wind balance. In turn, the strengthened upper-level flow favours enhanced large-scale ascent, providing an additional pathway for rainfall intensification and helping explain why the

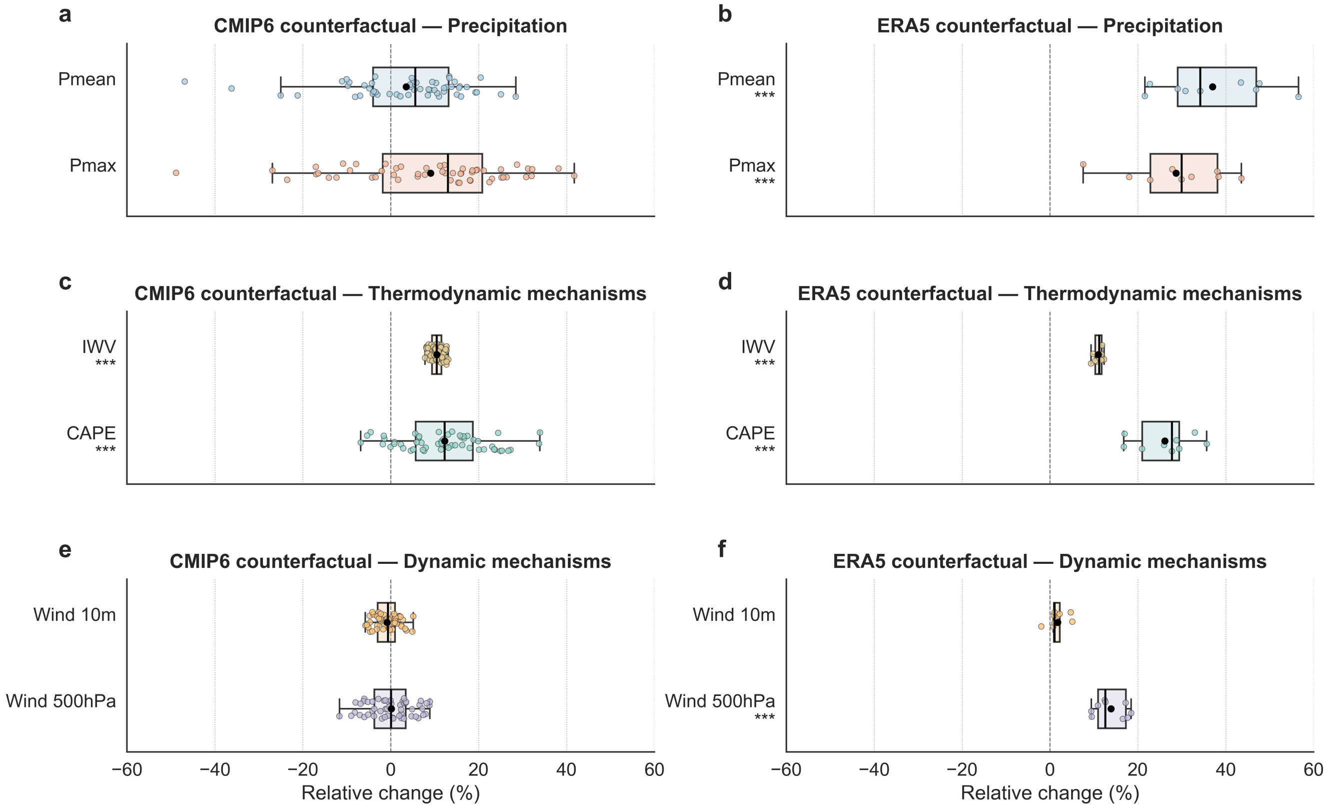

Figure 5. Relative changes (factual minus counterfactual, expressed as a fraction of the factual event, $(F - C)/F \times 100$) in precipitation (Pmean, Pmax), thermodynamic (IWV, CAPE) and dynamic (Wind 10 m, Wind 500 hPa) variables. Left column: CMIP6-past counterfactual ($n = 54$). Right column: ERA5-past counterfactual ($n = 9$). All values averaged over the Valencian Community (see Fig. S7). Asterisks denote statistical significance (one: $p < 0.05$, two: $p < 0.01$, three: $p < 0.001$), assigned only when $|\mathrm{SNR}| \geq 1$ to avoid flagging trivially small signals (see Methods).

increase in precipitation exceeds what would be expected from thermodynamic factors (IWV and CAPE) alone. Moreover, the resulting increase in vertical wind shear can promote more organized and longer-lived convection, consistent with the severe convective behaviour observed during the event, including numerous tornado reports (AEMET, 2024).

It is worth noting that this dynamical response emerges naturally from our experimental design. Our storyline approach preserves the synoptic context of the event through lagged initialisations 24–48 hours before the main day of the event, sufficient for the large-scale circulation to remain close to that of the observed storm but long enough for the atmosphere to adjust to the new thermodynamic background. Critically, we do not apply spectral nudging (in contrast to e.g. Sánchez-Benítez et al., 2022; Athanase et al., 2024; Insua-Costa et al., 2024; Campos et al., 2025), so the dynamical response is free to develop self-consistently with the imposed thermodynamic perturbation. Storyline attribution is typically framed as a highly conditioned approach to dynamics; here, we deliberately relax the degree of dynamical conditioning while still preserving the storyline framing. This lower degree of conditioning—which lets the counterfactual atmosphere evolve under its own physical balance—is what allows the wind response in Fig. 5f to emerge, and it is consistent with the thermal-wind argument outlined above. By contrast, more tightly nudged setups would suppress this dynamical adjustment by construction.

3.5 Future counterfactuals from observational trends

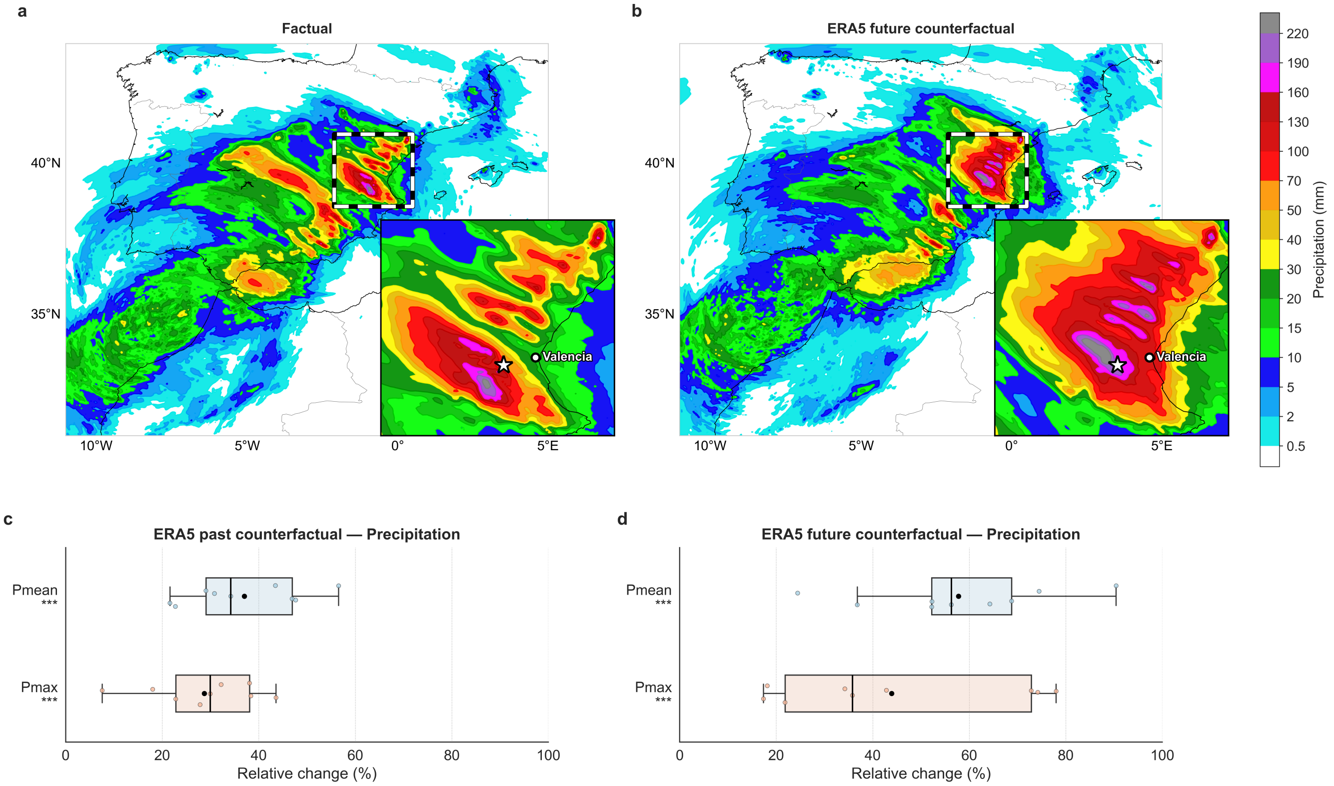

Figure 6. (a, b) 24-h accumulated precipitation on 29 October 2024 for the factual ensemble and the ERA5-future counterfactual, with a zoom-in over the Valencian region; the star marks Turís. (c, d) Boxplots of the relative change in spatially aggregated Pmean and Pmax for the ERA5-past counterfactual ($F - C_{\mathrm{past}}$ relative to F) and the ERA5-future counterfactual ($C_{\mathrm{future}} - F$ relative to F). The common reference is the factual event, so the past and future panels can be compared on the same scale. Asterisks denote statistical significance as in Fig. 5.

A natural extension of the ERA5-based approach is to construct future counterfactuals by adding the ERA5-derived warming signal—the same 1940–2024 trend used to build the past counterfactual—to the initial conditions of the attribution experiments, rather than subtracting it. We note that this is one feature where the ERA5-based methodology does not match the flexibility of CMIP6-based methods, which rely on multi-decadal climate-model projections forced by specific SSP scenarios. Although the ERA5 approach cannot represent specific socio-economic emission pathways, it does allow the construction of physically

https://doi.org/10.5194/egusphere-2026-3044
Preprint. Discussion started: 4 June 2026

plausible future scenarios; for instance, doubling the present-day warming signal corresponds to a plausible level of additional warming consistent with mid-range SSP scenarios for the late 21st century, and therefore provides a useful first-order benchmark of how the same event would unfold under a warmer climate.

A direct comparison between ERA5- and CMIP6-derived future counterfactuals—analogous to the past-to-present comparison shown in Sects. 3.3 and 3.4—is less straightforward. For the past, both approaches estimate the same physical quantity (the historical warming signal) and can therefore be compared on equal terms. For the future, by contrast, the two approaches describe conceptually distinct targets, as noted above. This conceptual mismatch, combined with the substantial computational cost of running an additional 54-member CMIP6-future ensemble, is why our future analysis is limited to the ERA5 case.

The corresponding nine-member ERA5-future counterfactual ensemble shows that the synoptic configuration of the event is again preserved, although the 500-hPa geopotential heights rise further to adjust to the warmer background state (Fig. S10). Extreme rainfall, however, intensifies substantially beyond its past-to-present response. Median 24-h changes in spatially aggregated precipitation over the Valencian Community reach $+57\,\%$ (IQR $[+52,+68]$) for Pmean and $+39\,\%$ (IQR $[+25,+66]$) for Pmax (Fig. 6c, d), notably larger than the corresponding past-to-present ERA5 increases of $+34\,\%$ and $+30\,\%$ (Sect. 3.4). The future ensemble exhibits noticeably larger dispersion than the past one, especially for Pmax, but the responses remain statistically significant. Given that the future warming signal is identical to the past-to-present one, this disproportionate response points to a nonlinear amplification of precipitation extremes under continued warming, which is particularly relevant from an impact perspective. The robustness of these future increases to alternative accumulation windows and spatial masks is documented in Sect. 4.2.

4 Limitations and generalisation

4.1 Methodological consistency of the warming signal

A potential methodological concern of our setup is the asymmetry between how the CMIP6 and ERA5 warming signals are derived. The CMIP6 perturbation follows the canonical delta approach (2009–2039 minus 1850–1880), the most widely used method in EEA (Schär et al., 1996), whereas the ERA5 perturbation is based on the 1940–2024 linear trend (see Methods). To assess whether this methodological difference could itself drive the contrast in attribution outcomes, we recomputed the CMIP6 multi-model warming using exactly the same 1940–2024 trend procedure used for ERA5 (Fig. 7). The CMIP6 delta and CMIP6 trend estimates closely match across the three pressure levels analysed, differing only slightly in magnitude while preserving the spatial structure, with their globally averaged magnitudes agreeing to within $\sim$10 %.

Although Fig. 7 shows just two visually similar panels, this seemingly innocuous agreement carries two implications that are central to our argument. First, it directly addresses the concern that a multi-decadal linear trend could be contaminated by internal variability: over a record as long as 1940–2024, internal variability averages out and the trend is dominated by the forced response, which is precisely why it reproduces the canonical pre-industrial-to-present delta so closely. Second, and more importantly, the equivalence between a model-based pre-industrial baseline and a 1940-onward observational trend opens the possibility of constructing anthropogenic warming signals for EEA without recourse to numerical climate models, relying

https://doi.org/10.5194/egusphere-2026-3044
Preprint. Discussion started: 4 June 2026

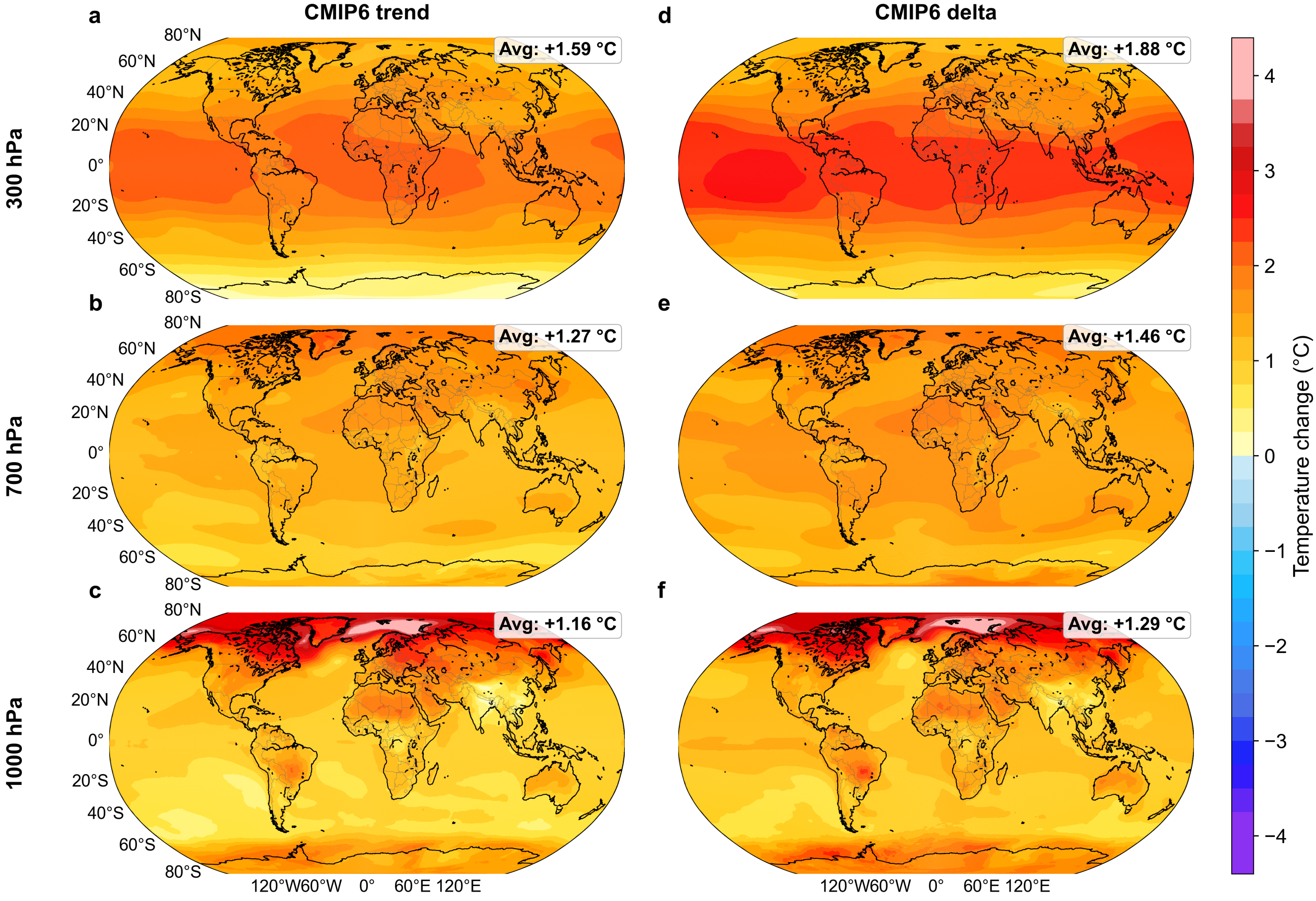

Figure 7. CMIP6 multi-model mean warming at 300, 700 and 1000 hPa computed as a linear trend over 1940–2024 (left) and as the difference between 30-year climatologies 2009–2039 minus 1850–1880 (right).

instead on observationally anchored estimates such as reanalyses. The ERA5 trend can therefore be regarded as a physically meaningful—if slightly conservative—approximation of the observed anthropogenic warming signal.

The idea of building counterfactual climates from observed trends rather than from model-derived deltas is not entirely new: Meredith et al. (2015), for instance, perturbed sea surface temperatures using observed multi-decadal trends in their attribution study of the 2012 Krymsk extreme rainfall event. As far as we are aware, however, this strategy has so far been restricted to SST. Modifying only the surface, without a consistent atmospheric adjustment, can lead to vertically inconsistent temperature profiles. For example, a cooler ocean below an unchanged warm troposphere in past counterfactuals would artificially enhance static stability and inhibit convection. This limitation is particularly relevant in short simulations, where the atmosphere may not have time to equilibrate with the imposed SST. Our framework extends this approach by applying observed trends consistently to all relevant three-dimensional and surface thermodynamic fields, ensuring vertical consistency from the outset.

Even with this internal consistency check and the additional support from the Palma radiosonde discussed in Sect. 3.2, ERA5 itself remains an imperfect representation of the true atmospheric state, particularly in earlier decades and over regions with sparse in-situ coverage. For the Valencia case, the consistency between ERA5 and the Palma sounding gives us high confidence that the ERA5-based attribution is much closer to the true response than the CMIP6-based one. However, the attributed response is strongly sensitive to the structure of the warming signal, differing by a factor of three between the CMIP6 and ERA5 cases. It is therefore plausible that even an ERA5-based attribution may deviate from the true response in other events or regions, particularly where reanalysis uncertainty is larger or no equivalent in-situ benchmark is available. Our framework therefore narrows the gap between pure model-based attribution and reality, but does not eliminate it.

4.2 Sensitivity to methodological choices

The relative changes reported in Sects. 3.4 and 3.5 aggregate precipitation over the Valencian Community administrative mask (Fig. S7b), use a 24-h accumulation window centred on 29 October 2024, and adopt the $(F-C)/F$ normalisation (Eq. 2). All three choices are defensible but represent specific methodological options, and the robustness of the headline numbers to these choices warrants explicit assessment. We address this with a three-dimensional sensitivity test on the precipitation response, summarised in Fig. S1, which spans (i) accumulation windows of 1, 3, 6, 12, and 24 h; (ii) two distinct spatial masks (the Valencian Community mask, and the intersection of the Fig. 4 zoom box with land, which captures the core of the modelled convective system); and (iii) the two delta formulations $(F-C)/F$ and $(F-C)/C$.

Several robust features emerge. The qualitative ordering ERA5-future $>$ ERA5-past $>$ CMIP6-past holds for every combination of window, mask, and (where applicable) formulation. In particular, ERA5-past responses are several times larger than CMIP6-past responses across all configurations tested, so the contrast between the two warming signals is not an artefact of any specific methodological choice.

The dependence on the accumulation window is markedly different between past and future cases. For the ERA5-future ensemble, median Pmean changes grow as the window shortens (from $\sim$+56 % at 24 h to $\sim$+86 % at 1 h on the Valencian Community mask), consistent with the well-documented super-Clausius–Clapeyron scaling of sub-daily convective rainfall. For the ERA5-past and CMIP6-past ensembles, however, the trend is reversed: median changes are larger at longer accumulation windows (e.g. +34 % at 24 h vs. +21 % at 1 h for ERA5-past; +6 % vs. -2 % for CMIP6-past). One possibility is that, for the past-counterfactual experiments, the imposed warming enhances the persistence of the event, so that longer accumulation windows integrate a larger response. We cannot tell from this analysis alone, however, whether this past/future contrast in window dependence is a general feature or specific to this event and setup.

The choice of normalisation has a strong effect on the ERA5 magnitudes but barely changes the CMIP6 ones. For the 24-h Valencian Community case, the CMIP6-past median Pmean changes by a negligible amount under the alternative formulation (from $+6\%$ under $(F-C)/F$ to $+6\%$ under $(F-C)/C$), whereas the ERA5-past median shifts from $+34\%$ to $+52\%$. This sensitivity is a direct algebraic consequence of the size of Δ itself: when F and C are close, as for the small CMIP6 response, the choice of denominator is inconsequential, whereas the larger ERA5 response makes F and C notably different and amplifies the dependence on the normalisation. We retain $(F-C)/F$ as the main metric for the reasons given in Methods.

Finally, the spatial mask introduces only minor changes, with one mild caveat in the future case. For 24-h Pmean on the Valencian Community vs. the Fig. 4 zoom-box-land mask, CMIP6-past medians are essentially unchanged ($+6\,\%$ vs. $+3\,\%$), as are ERA5-past responses ($+34\,\%$ vs. $+36\,\%$), while ERA5-future responses become smaller ($+56\,\%$ vs. $+40\,\%$). All main conclusions of this study remain unchanged by the choice of spatial mask.

4.3 Generalisation beyond Valencia

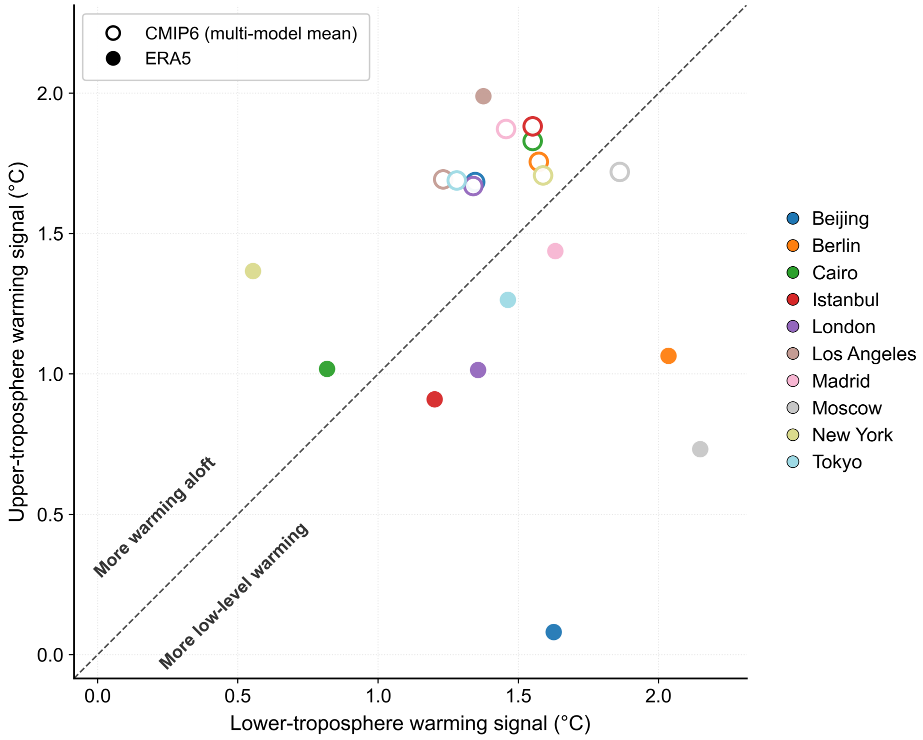

Figure 8. Lower-tropospheric vs upper-tropospheric warming signal at ten Northern Hemisphere mid-latitude cities, comparing ERA5 (filled circles) and CMIP6 multi-model means (open circles). The dashed line marks $y = x$. Warming signals are constructed as annual means using the same CMIP6 delta and ERA5 trend procedures described in Sect. 2.2, but without conditioning on any specific event timing.

Beyond the Valencia case, the underlying mechanism is not event-specific. Fig. 8 summarizes the warming signals that would be imposed in EEA experiments for ten mid-latitude cities in the Northern Hemisphere, where observational coverage is denser and reanalysis-based trends are more reliable. In CMIP6, all cities except one show stronger warming aloft than near the surface, whereas in ERA5, seven of the ten cities show stronger lower-tropospheric warming. The CMIP6 profiles are also more tightly clustered, indicating a comparatively uniform warming structure, while the ERA5 profiles exhibit greater spread, reflecting larger horizontal contrasts, in agreement with the results in Fig. 2 and Fig. 3b. The Valencia case therefore serves

https://doi.org/10.5194/egusphere-2026-3044
Preprint. Discussion started: 4 June 2026

as a test bed for a broader structural tendency: in many mid-latitude settings, using CMIP6-derived warming in attribution is likely to produce weaker precipitation responses than an observationally constrained warming structure.

This generalisation, however, comes with an important geographical caveat. The mid-latitude pattern documented in Fig. 8 is consistent with the broader structural biases identified in Fig. 2, but is not universal. In regions where the bias goes in the opposite direction (i.e. CMIP6 overestimating lower-tropospheric warming or underestimating upper-tropospheric warming), the same mechanism would operate with the opposite sign: CMIP6-based attribution would probably overestimate, rather than underestimate, the anthropogenic contribution to extreme precipitation.

Beyond this potential geographical extrapolation, our results may also carry broader implications for EEA as a field. Although our analysis focuses on a storyline framework, the biases identified imply that any EEA methodology relying on CMIP6-derived warming patterns is subject to similar systematic errors. Likewise, because the identified biases affect fundamental aspects of atmospheric stability and dynamics, their implications may extend beyond extreme rainfall to other types of extreme events.

4.4 Comparison with concurrent attribution studies

Three concurrent attribution studies of the same event have recently appeared in the literature (Barriopedro et al., 2025; Calvo-Sancho et al., 2026; Campos et al., 2025), all adopting a storyline approach and therefore directly comparable to ours. They converge on a positive anthropogenic contribution to the Valencia rainfall of about $\sim+20\,\%$. A direct comparison with our own figures, however, requires placing them on a common footing: the three studies normalise the response as $(\mathrm{F}-\mathrm{C})/\mathrm{C}$, whereas we adopt $(\mathrm{F}-\mathrm{C})/\mathrm{F}$. The sensitivity test in Sect. 4.2 shows that switching to $(\mathrm{F}-\mathrm{C})/\mathrm{C}$ leaves our CMIP6-based estimate essentially unchanged but pushes our ERA5-based one to about $\sim+50\,\%$. In this common metric, our ERA5-based response sits well above the $\sim+20\,\%$ reported by the other studies, so the underestimation under CMIP6-derived warming is preserved and, if anything, becomes more pronounced.

The comparison restricted to the CMIP6-based experiments is harder to reconcile. Since they share the same family of warming signals, one would expect closely matching responses. Yet our own ($<10\,\%$) is considerably smaller than the $\sim+20\,\%$ obtained by the other studies. This residual gap likely reflects methodological choices on which the experiments differ, including horizontal resolution, the number of ensemble members, the specific CMIP6 models used to build the warming signal, or the spatial aggregation mask. This spread, in any case, further illustrates the high sensitivity of attributed precipitation signals in this kind of study.

5 Conclusions

Our results demonstrate that the structure of anthropogenic warming exerts a first-order control on the attribution of extreme precipitation. CMIP6 and ERA5 agree on the global-mean magnitude of warming, but their three-dimensional distribution differs systematically: across the Northern Hemisphere, CMIP6 places relatively more warming aloft, whereas ERA5 shows stronger lower-tropospheric warming over land. When these contrasting structures are used to construct the factual and coun-

https://doi.org/10.5194/egusphere-2026-3044
Preprint. Discussion started: 4 June 2026

terfactual climates for the October 2024 Valencia storm, they lead to fundamentally different responses. The ERA5-based experiment yields enhanced low-level moistening, stronger convective instability and a more vigorous upper-level jet, producing a super-Clausius–Clapeyron precipitation response. The CMIP6-based experiment, with warming concentrated higher in the troposphere, reproduces these mechanisms only in attenuated form and yields a response close to or even below Clausius–Clapeyron scaling.

Looking ahead, the ERA5-future experiments show that the ERA5-based attribution framework remains applicable beyond the present-day case and reveal a clear non-linearity: for the same incremental warming, the precipitation response grows more strongly than in the past-to-present comparison, indicating that the super-Clausius–Clapeyron behaviour identified here is likely to become more pronounced under sustained warming.

Beyond the Valencia case, two further findings broaden the scope of the study. First, when applied to CMIP6, the 1940–2024 linear trend and the canonical 2009–2039 minus 1850–1880 delta yield warming signals of comparable magnitude and spatial structure, supporting the use of observationally derived trends as a model-independent basis for constructing counterfactual climates in EEA. Second, the structural mismatch documented for Valencia is also present across other Northern Hemisphere mid-latitude cities, suggesting that hypothetical EEA experiments performed at these locations could be subject to a similar underestimation as the one documented here.

In a context where the scientific and societal relevance of EEA continues to grow, our results offer an observation-based alternative for representing anthropogenic warming signals within storyline frameworks. Overall, our findings highlight that continued progress in attribution science requires advances not only in rapid or operational attribution capabilities, but also in the physical consistency and methodological rigour underpinning the construction of counterfactual worlds.

Code and data availability. ERA5 reanalysis data (Hersbach et al., 2020) were obtained from the Copernicus Climate Data Store (https://doi.org/10.24381/cds.6860a573 for monthly pressure-level data and https://doi.org/10.24381/cds.f17050d7 for monthly single-level data; both accessed 2025). CMIP6 historical and SSP2-4.5 simulations (Eyring et al., 2016) were retrieved from the Earth System Grid Federation (https://esgf-node.llnl.gov/projects/cmip6/). NCEP/DOE Reanalysis II is distributed by NOAA/PSL (https://psl.noaa.gov/data/gridded/data.ncep.reanalysis2.html). The Palma de Mallorca radiosonde record was downloaded from the NOAA Integrated Global Radiosonde Archive (IGRA, version 2; station SPM00008302; https://www.ncei.noaa.gov/products/weather-balloon/integrated-global-radiosonde-archive). The source code of the MPAS atmospheric model is publicly available at https://github.com/MPAS-Dev/MPAS-Model (Skamarock et al., 2012). The perturbation datasets used to initialise the counterfactual simulations, the MPAS model output analysed in this study, and the post-processing scripts producing the figures will be made publicly available on Zenodo upon acceptance of the manuscript (DOI to be assigned). In the meantime, they are available from the corresponding author on reasonable request.

Author contributions. D.I.C. designed the study, performed the pseudo-global-warming simulations, produced the figures, and wrote the first manuscript draft. M.L.C. and M.S.R. made decisive contributions to the initial conceptualization of the study and the design of the

numerical experiments. V.M.H.D. supported the data analysis and interpretation. J.L.G. and D.G.M., along with all co-authors, contributed ideas, interpretation of the results, and manuscript revisions.

Competing interests. The authors declare that they have no competing interests.

Acknowledgements. D.I.C. is supported by the Research Foundation–Flanders (FWO) under grant no. 12A0Z26N. M.L.C. was funded by the Autonomous Province of Bozen/Bolzano–South Tyrol through the Seal of Excellence project HIPEAtMount (D53C24001140003). D.G.M., V.M.H.D. and J.L.G. acknowledge support from the European Research Council (ERC) through the HEAT Consolidator Grant (grant agreement 101088405). The simulations and analyses made use of the infrastructure of the Vlaams Supercomputer Centrum (VSC) in Ghent, Belgium. We acknowledge the use of Claude Code (Anthropic) for assistance with figure-generation code and manuscript editing. The numerical simulations, as well as all scientific analyses, interpretations, and conclusions, are those of the authors, who take full responsibility for the work.

References

AEMET: Estudio sobre la situación de lluvias intensas, localmente torrenciales y persistentes, en la península ibérica y Baleares entre los días 28 de octubre y 4 de noviembre de 2024, https://www.aemet.es/documentos/es/conocermas/recursos_en_linea/publicaciones_y_estudios/estudios/estudio_28_oct_4_nov_2024.pdf, accessed: 2025-11-03, 2024.

Allan, R. P. and Soden, B. J.: Atmospheric warming and the amplification of precipitation extremes, Science, 321, 1481–1484, https://doi.org/10.1126/science.1160787, 2008.

Athanase, M., Sánchez-Benítez, A., Monfort, E., Jung, T., and Goessling, H. F.: How climate change intensified storm Boris' extreme rainfall, revealed by near-real-time storylines, Communications Earth and Environment, 5, 676, https://doi.org/10.1038/s43247-024-01847-0, 2024.

Barriopedro, D., Jiménez-Esteve, B., Collazo, S., Garrido-Pérez, J. M., Johnson, N., and García-Herrera, R.: A Multimethod Attribution Analysis of Spain's 2024 Extreme Precipitation Event, Bulletin of the American Meteorological Society, 106, E2440–E2460, https://doi.org/10.1175/BAMS-D-25-0049.1, 2025.

Calvo-Sancho, C., Díaz-Fernández, J., González-Alemán, J. J., Halifa-Marín, A., Miglietta, M. M., Azorín-Molina, C., Prein, A. F., Montoro-Mendoza, A., Bolgiani, P., Morata, A., and Martín, M. L.: Human-induced climate change amplification on storm dynamics in Valencia's 2024 catastrophic flash flood, Nature Communications, 17, 1492, https://doi.org/10.1038/s41467-026-68929-9, 2026.

Campos, D. A., Grayson, K., Saurral, R. I., Beyer, S., John, A., Olmo, M., and Doblas-Reyes, F.: The October 2024 extreme precipitation event over Valencia: storyline attribution of the synoptic-scale thermodynamic drivers, EGUsphere preprint, https://doi.org/10.5194/egusphere-2025-5929, preprint, currently under review, 2025.

Casado, M., Hébert, R., Faranda, D., and Landais, A.: The quandary of detecting the signature of climate change in Antarctica, Nature Climate Change, 13, 1082–1088, https://doi.org/10.1038/s41558-023-01791-5, 2023.

Cattiaux, J., Vautard, R., Cassou, C., Yiou, P., Masson-Delmotte, V., and Codron, F.: Winter 2010 in Europe: a cold extreme in a warming climate, Geophysical Research Letters, 37, L20 704, https://doi.org/10.1029/2010GL044613, 2010.

Clarke, B., Otto, F., Stuart-Smith, R., and Harrington, L.: Extreme weather impacts of climate change: an attribution perspective, Environmental Research: Climate, 1, 012 001, https://doi.org/10.1088/2752-5295/ac6e7d, 2022.

Davy, R. and Esau, I.: Global climate models' bias in surface temperature trends and variability, Environmental Research Letters, 9, 114 024, https://doi.org/10.1088/1748-9326/9/11/114024, 2014.

Donat, M. G., Lowry, A. L., Alexander, L. V., O'Gorman, P. A., and Maher, N.: More extreme precipitation in the world's dry and wet regions, Nature Climate Change, 6, 508–513, https://doi.org/10.1038/nclimate2941, 2016.

Eyring, V., Bony, S., Meehl, G. A., Senior, C. A., Stevens, B., Stouffer, R. J., and Taylor, K. E.: Overview of the Coupled Model Intercomparison Project Phase 6 (CMIP6) experimental design and organization, Geoscientific Model Development, 9, 1937–1958, https://doi.org/10.5194/gmd-9-1937-2016, 2016.

Fan, Y., Chan, D., Zhang, P., and Li, L.: Disagreement on the North Atlantic cold blob formation mechanisms among climate models, Journal of Climate, 37, 4061–4078, https://doi.org/10.1175/JCLI-D-23-0654.1, 2024.

Faranda, D., Bourdin, S., Ginesta, M., Krouma, M., Noyelle, R., Pons, F., Yiou, P., and Messori, G.: A climate-change attribution retrospective of some impactful weather extremes of 2021, Weather and Climate Dynamics, 3, 1311–1340, https://doi.org/10.5194/wcd-3-1311-2022, 2022.

González-Alemán, J. J., Insua-Costa, D., Bazile, E., González-Herrero, S., Miglietta, M. M., Groenemeijer, P., and Donat, M. G.: Anthropogenic warming had a crucial role in triggering the historic and destructive Mediterranean derecho in summer 2022, Bulletin of the American Meteorological Society, 104, E1526–E1532, https://doi.org/10.1175/BAMS-D-23-0119.1, 2023.

Grell, G. A. and Freitas, S. R.: A scale and aerosol aware stochastic convective parameterization for weather and air quality modeling, Atmospheric Chemistry and Physics, 14, 5233–5250, https://doi.org/10.5194/acp-14-5233-2014, 2014.

Hersbach, H., Bell, B., Berrisford, P., Hirahara, S., Horányi, A., Muñoz-Sabater, J., Nicolas, J., Peubey, C., Radu, R., Schepers, D., Simmons, A., Soci, C., Abdalla, S., Abellan, X., Balsamo, G., Bechtold, P., Biavati, G., Bidlot, J., Bonavita, M., De Chiara, G., Dahlgren, P., Dee, D., Diamantakis, M., Dragani, R., Flemming, J., Forbes, R., Fuentes, M., Geer, A., Haimberger, L., Healy, S., Hogan, R. J., Hólm, E., Janisková, M., Keeley, S., Laloyaux, P., Lopez, P., Lupu, C., Radnoti, G., de Rosnay, P., Rozum, I., Vamborg, F., Villaume, S., and Thépaut, J.-N.: The ERA5 global reanalysis, Quarterly Journal of the Royal Meteorological Society, 146, 1999–2049, https://doi.org/10.1002/qj.3803, 2020.

Hong, S.-Y. and Lim, J. O. J.: The WRF single-moment 6-class microphysics scheme (WSM6), Journal of the Korean Meteorological Society, 42, 129–151, 2006.

Hong, S.-Y., Noh, Y., and Dudhia, J.: A new vertical diffusion package with an explicit treatment of entrainment processes, Monthly Weather Review, 134, 2318–2341, https://doi.org/10.1175/MWR3199.1, 2006.

Insua-Costa, D., Lemus-Cánovas, M., González-Alemán, J. J., Senande-Rivera, M., Llasat, M. d. C., Miguez-Macho, G., and Miralles, D. G.: Extraordinary 2021 snowstorm in Spain reveals critical threshold response to anthropogenic climate change, Communications Earth and Environment, 5, 339, https://doi.org/10.1038/s43247-024-01503-7, 2024.

John, A., Beyer, S., Athanase, M., Sánchez-Benítez, A., Goessling, H. F., Hossain, A., et al.: Global kilometre-scale climate storylines using spectral nudging, Journal of Advances in Modeling Earth Systems, https://doi.org/10.1029/2025MS005326, 2026.

Keil, P., Schmidt, H., Stevens, B., and Bao, J.: Variations of tropical lapse rates in climate models and their implications for upper tropospheric warming, Journal of Climate, 34, 9747–9761, https://doi.org/10.1175/JCLI-D-21-0196.1, 2021.

Masson-Delmotte, V. et al., eds.: Climate Change 2021: The Physical Science Basis. Contribution of Working Group I to the Sixth Assessment Report of the Intergovernmental Panel on Climate Change, Cambridge University Press, https://doi.org/10.1017/9781009157896, 2021.

Meredith, E. P., Semenov, V. A., Maraun, D., Park, W., and Chernokulsky, A. V.: Crucial role of Black Sea warming in amplifying the 2012 Krymsk precipitation extreme, Nature Geoscience, 8, 615–619, https://doi.org/10.1038/ngeo2483, 2015.

Min, S.-K., Zhang, X., Zwiers, F. W., and Hegerl, G. C.: Human contribution to more-intense precipitation extremes, Nature, 470, 378–381, https://doi.org/10.1038/nature09763, 2011.

Mitchell, D. M., Lo, Y. T. E., Seviour, W. J. M., Haimberger, L., and Polvani, L. M.: The vertical profile of recent tropical temperature trends: Persistent model biases in the context of internal variability, Environmental Research Letters, 15, 104 008, https://doi.org/10.1088/1748-9326/ab9af7, 2020.

Mueller, B. and Seneviratne, S. I.: Systematic land climate and evapotranspiration biases in CMIP5 simulations, Geophysical Research Letters, 41, 128–134, https://doi.org/10.1002/2013GL058055, 2014.

Ossó, A., Craig, P., and Allan, R. P.: An assessment of CMIP6 climate signals and biases in temperature, precipitation and soil moisture over Europe, International Journal of Climatology, 43, 5698–5719, https://doi.org/10.1002/joc.8169, 2023.

Pall, P., Aina, T., Stone, D. A., Stott, P. A., Nozawa, T., Hilberts, A. G. J., Lohmann, D., and Allen, M. R.: Anthropogenic greenhouse gas contribution to flood risk in England and Wales in autumn 2000, Nature, 470, 382–385, https://doi.org/10.1038/nature09762, 2011.

Pithan, F. and Mauritsen, T.: Arctic amplification dominated by temperature feedbacks in contemporary climate models, Nature Geoscience, 7, 181–184, https://doi.org/10.1038/ngeo2071, 2014.

Sánchez-Benítez, A., Goessling, H., Pithan, F., Semmler, T., and Jung, T.: The July 2019 European heat wave in a warmer climate: storyline scenarios with a coupled model using spectral nudging, Journal of Climate, 35, 2373–2390, https://doi.org/10.1175/JCLI-D-21-0573.1, 2022.

Santer, B. D., Wigley, T. M. L., Mears, C., Wentz, F. J., Klein, S. A., Seidel, D. J., Taylor, K. E., Thorne, P. W., Wehner, M. F., Gleckler, P. J., Boyle, J. S., Collins, W. D., Dixon, K. W., Doutriaux, C., Free, M., Fu, Q., Hansen, J. E., Jones, G. S., Ruedy, R., Karl, T. R., Lanzante, J. R., Meehl, G. A., Ramaswamy, V., Russell, G., and Schmidt, G. A.: Amplification of surface temperature trends and variability in the tropical atmosphere, Science, 309, 1551–1556, https://doi.org/10.1126/science.1114867, 2005.

Schär, C., Frei, C., Lüthi, D., and Davies, H. C.: Surrogate climate-change scenarios for regional climate models, Geophysical Research Letters, 23, 669–672, https://doi.org/10.1029/96GL00265, 1996.

Shepherd, T. G.: A common framework for approaches to extreme event attribution, Current Climate Change Reports, 2, 28–38, https://doi.org/10.1007/s40641-016-0033-y, 2016.

Shepherd, T. G., Boyd, E., Calel, R. A., Chapman, S. C., Dessai, S., Dima-West, I. M., Fowler, H. J., James, R., Maraun, D., Martius, O., Senior, C. A., Sobel, A. H., Stainforth, D. A., Tett, S. F. B., Trenberth, K. E., van den Hurk, B. J. J. M., Watkins, N. W., Wilby, R. L., and Zenghelis, D. A.: Storylines: an alternative approach to representing uncertainty in physical aspects of climate change, Climatic Change, 151, 555–571, https://doi.org/10.1007/s10584-018-2317-9, 2018.

Sillmann, J., Shepherd, T. G., van den Hurk, B., Hazeleger, W., Martius, O., Slingo, J., and Zscheischler, J.: Event-based storylines to address climate risk, Earth's Future, 9, e2020EF001 783, https://doi.org/10.1029/2020EF001783, 2021.

Simmons, A. J.: Trends in the tropospheric general circulation from 1979 to 2022, Weather and Climate Dynamics, 3, 777–809, https://doi.org/10.5194/wcd-3-777-2022, 2022.

Skamarock, W. C., Klemp, J. B., Duda, M. G., Fowler, L. D., Park, S.-H., and Ringler, T. D.: A multiscale nonhydrostatic atmospheric model using centroidal Voronoi tesselations and C-grid staggering, Monthly Weather Review, 140, 3090–3105, https://doi.org/10.1175/MWR-D-11-00215.1, 2012.

Soci, C., Hersbach, H., Simmons, A., Poli, P., Bell, B., Berrisford, P., Horányi, A., Muñoz-Sabater, J., Nicolas, J., Radu, R., Schepers, D., Villaume, S., Haimberger, L., Woollen, J., Buontempo, C., and Thépaut, J.-N.: The ERA5 global reanalysis from 1940 to 2022, Quarterly Journal of the Royal Meteorological Society, 150, 4014–4048, https://doi.org/10.1002/qj.4803, 2024.

Stott, P. A., Stone, D. A., and Allen, M. R.: Human contribution to the European heatwave of 2003, Nature, 432, 610–614, https://doi.org/10.1038/nature03089, 2004.

Stott, P. A., Christidis, N., Otto, F. E. L., Sun, Y., Vanderlinden, J.-P., van Oldenborgh, G. J., Vautard, R., von Storch, H., Walton, P., Yiou, P., and Zwiers, F. W.: Attribution of extreme weather and climate-related events, WIREs Climate Change, 7, 23–41, https://doi.org/10.1002/wcc.380, 2016.

Thorne, P. W., Lanzante, J. R., Peterson, T. C., Seidel, D. J., and Shine, K. P.: Tropospheric temperature trends: History of an ongoing controversy, WIREs Climate Change, 2, 66–88, https://doi.org/10.1002/wcc.80, 2011.

van Garderen, L., Feser, F., and Shepherd, T. G.: A methodology for attributing the role of climate change in extreme events: a global spectrally nudged storyline, Natural Hazards and Earth System Sciences, 21, 171–186, https://doi.org/10.5194/nhess-21-171-2021, 2021.

Yuan, S. and Quiring, S. M.: Evaluation of soil moisture in CMIP5 simulations over the contiguous United States using in situ and satellite observations, Hydrology and Earth System Sciences, 21, 2203–2218, https://doi.org/10.5194/hess-21-2203-2017, 2017.

Zebaze, S., Anand, A., Fotso-Nguemo, T. C., Taguela, T. N., Ngavom, Z., Komkoua Mbienda, A. J., Fotso-Kamga, G., Choumbou, P. C., and Vondou, D. A.: Assessing the performance of the CMIP6 multi model mean in simulating precipitation and temperature across Africa, Modeling Earth Systems and Environment, 11, 374, https://doi.org/10.1007/s40808-025-02560-3, 2025. 570